PHYSICAL REVIEW B **100**, 224510 (2019)

Origin of hour-glass magnetic dispersion in underdoped cuprate superconductors

Y. A. Kharkov and O. P. Sushkov
School of Physics, University of New South Wales, Sydney 2052, Australia

(Received 16 January 2019; revised manuscript received 14 September 2019; published 13 December 2019)

In this work we explain the hour-glass magnetic dispersion in underdoped cuprates. The dispersion arises due to the Lifshitz-type magnetic criticality. Superconductivity also plays a role, but the role is secondary. We list six major experimental observations related to the hour glass and explain all of them. The theory provides a unified picture of the evolution of magnetic excitations in various cuprate families, including "hour-glass" and "wine-glass" dispersions and an emergent static incommensurate order. We propose the Lifshitz spin-liquid "fingerprint" sum rule, and show that the latest data confirm the validity of the sum rule.

DOI: 10.1103/PhysRevB.100.224510

I. INTRODUCTION

The "hour-glass" (HG) dispersion, observed in inelastic neutron scattering, is a generic property of hole-doped high-temperature cuprate superconductors [1–5] (for a review see Ref. [6]). The dispersion shown in Fig. 1(a) consists of the upper and the lower branches, the so-called (π,π) "spin resonance" separates the two branches. In this work, we shift momentum origin to (π,π) [see Fig. 2(a)], so our $q=0$ corresponds to (π,π) in neutron scattering. This shift is convenient for theory and quite often is used in neutron scattering papers. The HG dispersion is a major effect of strong electron correlations. While there is a general feeling that the upper part of the HG is due to localized spins and the lower part is related to itinerant holes [6,7], there is no understanding of the mechanism of this phenomenon in spite of two decades of efforts. There are a set of observations that must be explained, and they are as follows:

(O1) The lower part of the HG shrinks to zero when doping is decreasing, $x\rightarrow 0$ [6].

(O2) In optimally doped cuprates, $x\approx 0.15$, the lower part of the HG is observed in the superconducting (SC) state and disappears in the normal (N) state [8].

(O3) Contrary to (O2), in underdoped cuprates the lower part of HG is almost the same or exactly the same in the SC state and the N state just above T_c [6,9–11]. Moreover, the HG and the (π,π) resonance were recently observed [12] in the insulating $La_{2-x}Sr_xCuO_4$ at $x=0.0192$ where SC does not exist.

(O4) The upper part of HG is always almost the same in the SC state and in the N state, and the slope of the upper part decreases with doping [Fig. 1(a)].

(O5) In heavily underdoped cuprates, the lower part of HG propagates down to zero energy resulting in an emergent static incommensurate magnetic order [13,14].

(O6) All cuprate families are microscopically similar, values of the superexchange and hopping matrix elements are close. At the same time, details of the lower part of the HG dispersion vary across different cuprate families. Moreover, in underdoped $HgBa_2CuO_{4+\delta}$ the HG evolves to the "wine glass" [11,15].

Theoretical models of the magnetic dispersion and the (π,π) resonance are split into two classes, models based on the normal Fermi-liquid picture with a large Fermi surface and usual electrons with spin [17–21], and models based on the picture of a doped Mott insulator with a small Fermi surface and spinless holons [22,23]. All early models have been motivated by experiment [8] in optimally doped $YBa_2Cu_3O_7$ and belong to the first class. In this approach, the (π,π) resonance is explained as a spin exciton in the d-wave SC phase. These models are consistent with observation (O2), but inconsistent with all other observations which appeared later and that indicate that SC is not essential. In light of this inconsistency, the spin exciton model was modified by artificial introduction of localized spins in the normal Fermi-liquid model [19,21]. This modification partially explains the observation (O4) [in addition to (O2)], but is still inconsistent with all other observations.

The second theoretical approach based on the picture of a doped Mott insulator was developed later after the low-doping data were obtained. This approach naturally explains the observation (O1). The model of Ref. [22] is based on the picture of static spin spiral [24]. This model explains the observations (O1), (O3), (O5), but fails in all other points. The model of Ref. [23] explains (O1) and partially (O4), but fails in all other points. Thus, the theoretical situation is unsatisfactory.

In this work we pursue the approach of a lightly doped Mott insulator. There are four major experimental facts supporting the Mott insulator approach, and they are as follows:

(F1) According to NMR, the nearest-site antiferromagnetic exchange $J\approx 125$ meV is doping independent [25].

(F2) The second fact is the observation (O1) from the HG list presented above. It is hardly possible to shrink the HG to zero at zero doping in any model but doped Mott insulator.

(F3) Resonant inelastic x-ray scattering (RIXS) data indicate that the high-energy magnons, $\omega\sim 200$–300 meV, in doped compounds are practically the same as in undoped ones, this includes both the dispersion and the spectral weight [26].

(F4) The momentum-integrated structure factor $S(\omega)$ measured in neutron scattering at $\omega\approx 50$–80 meV in doped

©2019 American Physical Society

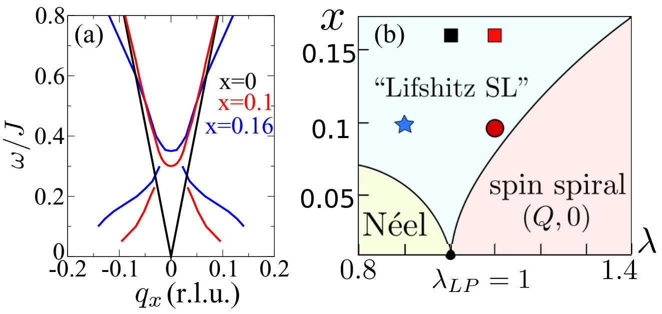

FIG. 1. (a) Theoretical HG dispersions for $\lambda = 1.1$ and for two values of doping, $x = 0.1$ (red) and $x = 0.16$ (blue). The black line represents the magnon dispersion in the parent undoped compound ($x = 0$). (b) Zero-temperature λ-x phase diagram of extended t-J model consists of three phases, Néel, Lifshitz spin liquid, spin spiral [16]. The tricritical Lifshitz point is $\lambda = 1$, $x = 0$. The squares, the circle, and the star are the points considered in the text as examples (r.l.u. = reciprocal lattice units).

compounds is practically the same as in undoped ones. We will demonstrate this observation at the end of this paper.

These four facts unambiguously favor the Mott insulator approach. The Mott insulator approach necessarily implies a small Fermi surface [Fig. 2(a)] and this immediately leads to two conclusions that are evident without calculations. The *first* conclusion concerns superconductivity. The Fermi energy is proportional to the doping x, $\epsilon_F \sim xJ$. For optimal doping, $x = 0.15$, the Fermi energy is $\epsilon_F \approx 35$ meV. On the other hand, we know experimentally that the superconducting gap is $\Delta_{SC} \approx 30$ meV. Thus, all cuprates are in the strong coupling limit $\epsilon_F \approx \Delta_{SC}$. The *second* conclusion concerns the spin-liquid ground state. Consistently with small Fermi surface the number of charge carriers measured via Hall effect is equal to the doping $x \ll 1$. The number of uncompensated spins in a doped Mott insulator is $1 - x$, so unlike a normal metal the number of spins is much larger than the number of charge carriers. We also know that the static magnetic order disappears above several percent doping, when $x \ll 1 - x$. These points indicate that spin and charge are separated and that quantum spin fluctuations "melt" the static magnetic order to a spin liquid (SL). Of course, the notion of SL in cuprates is not new, the same motivation is behind the resonating valence bond (RVB) SL model [27].

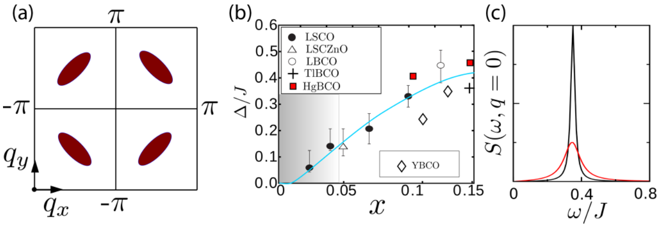

FIG. 2. (a) Small Fermi surface and momenta q_x, q_y for magnetic scattering. (b) The spin-liquid gap versus doping (cyan line) [16]. The theoretical curve corresponds to $\lambda = 1$. Points show experimental data. In different compounds, values of λ can be somewhat different and this explains scattering of experimental points. (c) The ω scan of the spectral function at $q = 0$. The black solid line illustrates the perfect δ function, and the dashed red line shows the temperature (disorder) broadened line.

This work is based on the recent progress in understanding of the SL state of cuprates [16]. The SL in cuprates is different to the RVB model. It is the quantum critical Ioffe-Larkin–type SL ("Lifshitz SL") [16]. This insight allows us to perform calculations and to explain all properties of the HG. There are the following sections in the paper. Section II gives the magnetic response in the spin-liquid phase. In Sec. III, calculated q scans of the spectral function at optimal doping are discussed and in Sec. IV outlines the magnetic criticality mechanism of the hour-glass dispersion. In Sec. V, the following question is addressed: Is there a hole in the hour glass? In Sec. VI, calculated q scans of the spectral function in the underdoped case and emergent incommensurate magnetic order are addressed. In Sec. VII the wine-glass dispersion and in Sec. VIII the Lifshitz spin-liquid fingerprint relation are discussed. Conclusions are given in Sec. IX. Technical details are presented in the Appendices.

II. MAGNETIC RESPONSE IN THE SPIN-LIQUID PHASE

We start with the zero-temperature λ-x phase diagram from Ref. [16] presented in Fig. 1(b). The dimensionless parameter λ defined as

$$\lambda = \frac{2g^2 m^*}{\pi \rho_s} \tag{1}$$

plays a crucial role in the theory, it controls magnetic criticality. Here, m^* is the holon effective mass, ρ_s is bare spin stiffness, and g is the holon-magnon coupling constant. The Lifshitz quantum tricritical point is $\lambda = 1$, $x = 0$. Three phases meet at the tricritical point, the collinear Néel phase, Lifshitz SL, the spin spiral state, see Appendix B. The Lifshitz SL is characterized by a parameter Δ that we term the SL gap. It is worth noting that in the exact sense the SL is gapless. Below we also introduce and explain the spin pseudogap Δ_s. Aside from the Lifshitz quantum tricritical point, there is another critical point $\lambda = 2$ related to the phase separation. Our analysis is based on the extended t-J model which is described by the antiferromagnetic exchange $J \approx 125$ meV and hopping parameters. The relation between parameters of the extended t-J model and λ is discussed in Appendix A 1. Having the nearest-site hopping parameter t fixed, $t/J \approx 3$, one can vary distant hopping parameters. In principle, this results in variation of λ in a very broad range, $0 < \lambda < \infty$. Using values of the hopping matrix elements obtained in local density approximation (LDA) calculations [28] one can obtain the following range for the criticality parameter $\sim 0.7 \leqslant \lambda \leqslant 2$. Nevertheless, this range of λ is too wide, it is even sufficient to drive the system to the phase separation. Experiments indicate that most cuprates are magnetically disordered except of the emergent magnetism at very low doping. This observation allows us to restrict the range to approximately $\lambda = 1.1 \pm 0.3$ shown in Fig. 1(b). The criticality parameter λ can vary from one cuprate family to another and can slightly depend on doping. For more details regarding the derivation of the field-theoretical description of the extended t-J model, see Appendix A 2.

To avoid misunderstanding, we note that the magnetic criticality we are talking about is unrelated to the quantum critical point at doping $x = x^* \approx 0.2$ (the end point of the "pseudogap" regime) where presumably the small Fermi surface is transformed to the large one [29]. We only consider $x < x^*$ and claim that all hole-doped cuprates are close to the Lifshitz magnetic criticality. One can also call it the "hidden" criticality. It is hidden in the sense that unlike doping, the parameter λ cannot be directly measured.

The first message of our paper is that the HG dispersion is a direct consequence of the SL gap and the Lifshitz magnetic criticality. SC plays a secondary role, it only influences the particle-hole decay phase space and narrows the spectral lines in the lower part of HG. The first message resolves the generic problems (O1)–(O5) listed in the Introduction. The second message is that due to proximity to the quantum critical point a small ($\sim$10%) variation of λ results in sizable change of the lower part of HG. This explains the point (O6) from the observation list.

We introduce superconductivity in the theory *ad hoc* via the phenomenological d-wave SC gap

$$\Delta_{\boldsymbol{k}} = \Delta_{\rm SC}\tfrac{1}{2}(\cos k_x - \cos k_y). \tag{2}$$

For details, see Appendix C. In our theory, the (π, π) resonance (the neck of the HG) is unrelated to SC. The resonance is a manifestation of the SL gap Δ which is practically the same in the N state and in the SC state. Quite often in neutron scattering papers the energy of the neck of HG is denoted by $E_{\rm cross}$, this is the same as the SL gap, $\Delta = E_{\rm cross}$. The gap Δ was calculated in Ref. [16] and is plotted versus doping in Fig. 2(b). The scattering of experimental points in this plot is one of the manifestations of the observation (O6) which is explained by proximity to the magnetic criticality.

We describe magnetic response at energy $\omega \lesssim J$ in terms of fluctuating staggered magnetization $\vec{n}$. The Green's function of the $\vec{n}$ field in the SL phase reads, see Appendix A 3

$$D(\omega, \boldsymbol{q}) = \frac{16J\sqrt{1-\mu x}}{\omega^2 - c^2 q^2 - \Delta^2 - \Pi(\omega, \boldsymbol{q}) + i0}. \tag{3}$$

Here, Δ is the SL gap and $\Pi(\omega, q)$ is the magnon polarization operator. The magnon speed is $c \approx c_0\sqrt{1-\mu x}$, where $c_0 \approx \sqrt{2}J$ is the magnon speed in the undoped compound. The coefficient $\mu \approx 4$ has been calculated numerically within the t-J model [16]. The uncertainty of this calculation is about $4 < \mu < 5$. The coefficient μ determines the dispersion slope softening at high energy. The softening is known experimentally and therefore the value of μ can be also extracted from experimental data. This gives the same uncertainty interval $4 < \mu < 5$.

The magnetic spectral function is $S(\omega, \boldsymbol{q}) = -\frac{A}{16\pi J}{\rm Im}D$. The proportionality coefficient A depends on the onsite magnetic moment, Cu atomic form factor, etc. This coefficient is practically the same for all hole-doped cuprates, at least for the single-layer cuprates. The spectral function in the parent compound (Néel state, $x = 0$) is

$$S_{\text{Néel}}(\omega, \boldsymbol{q}) = A\delta\big(\omega^2 - c_0^2 q^2\big). \tag{4}$$

The holon polarization operator $\Pi(\omega, \boldsymbol{q})$ calculated in Appendix C is a complex function of ω and $\boldsymbol{q}$, however, $\Pi(\omega, 0) = 0$. Therefore, the spectral function at finite doping at $q = 0$, $S(\omega, 0) = A\sqrt{1-\mu x}\,\delta(\omega^2 - \Delta^2)$, is a perfect (π, π) resonance shown in Fig. 2(c). Impurities and finite temperature give rise to a broadening illustrated by the red dashed line in Fig. 2(b). Importantly, the spectral weight is independent of the broadening and is defined by the SL gap Δ in the particular compound:

$$W = \int_0^\infty S(\omega, 0)d\omega \approx \frac{A\sqrt{1-\mu x}}{2\Delta}. \tag{5}$$

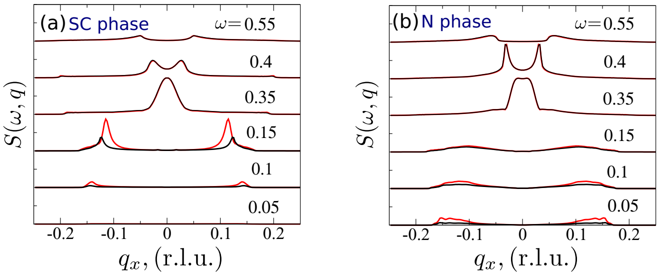

FIG. 3. Calculated momentum scans of the spectral function for $x = 0.16$, $\Delta = 0.35J$, $\Delta_{\rm SC} = 0.2J$ and six different energies. Energies in units of J are shown near the respective lines. (a) Corresponds to the SC state and (b) to the N state. Black curves correspond to $\lambda = 1$ and red curves correspond to $\lambda = 1.1$. Black and red practically coincide for higher energies.

III. CALCULATED q SCANS OF THE SPECTRAL FUNCTION AT OPTIMAL DOPING

In order to explain mechanism of the HG we consider separately the upper and the lower parts of the HG [see Fig. 1(a)]. In a crude approximation one can neglect the polarization operator in Eq. (3) for the upper part of the HG and this results in the dispersion

$$\omega_q \approx \sqrt{\Delta^2 + c_0^2(1-\mu x)q^2}. \tag{6}$$

Of course, we can do better than this crude approximation. In Fig. 3 we plot q_x scans of the spectral function calculated numerically [for definition of axes, see Fig. 2(a)]. The calculation accounts for the polarization operator and is performed for $x = 0.16$ and six values of ω. The value of the SL gap is taken from Fig. 2(b), $\Delta = 0.35J$, and $\Delta_{\rm SC} = 0.2J \approx 25$ meV (see Appendix C). Figure 3(a) corresponds to the SC state and Fig. 3(b) to the N state [30]. The plot demonstrates that the upper part of the HG, $\omega > \Delta$, is only weakly sensitive to SC in agreement with observation (O4). In both SC and N phases, the polarization operator gives a broadening and some asymmetry of peaks in the spectral function, but overall the upper part of HG is consistent with crude Eq. (6). On the other hand, according to Fig. 3 sharp peaks in the lower part of HG, $\omega < \Delta$, exist in the SC state and disappear in the N state in agreement with observation (O2). However, the peaks are still present in the N state, they just become very broad due to the decay to the particle-hole continuum. The spectra in Fig. 3(a) correspond to the HG dispersion plotted in Fig. 1(a) by the blue line. We plot the dispersion again in Fig. 4(a) with indication of SL gap Δ and the spin pseudogap Δ_s. According to Fig. 3(a) in the SC state the magnetic

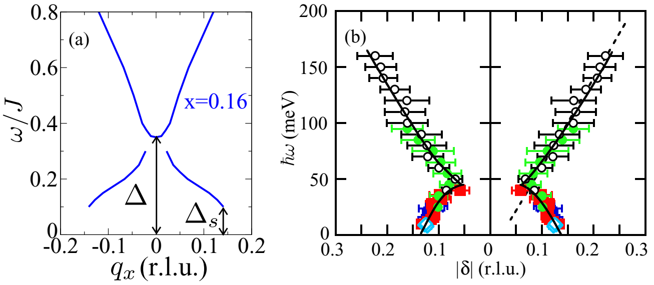

FIG. 4. (a) The HG dispersion for $x = 0.16$ deduced from spectra in Fig. 3(a). In this plot we indicate the SL gap Δ and the spin pseudogap Δ_s. (b) The HG dispersion in $La_{1.84}Sr_{0.16}CuO_4$ from Ref. [31].

response is strongly suppressed at low frequencies $\omega \lesssim 0.1J$. The suppression can be described by the spin pseudogap Δ_s indicated in Fig. 4(a). Unlike the true gap Δ, the Δ_s is a pseudogap since at the incommensurate q points there is some response down to zero energy. In the N state [Fig. 3(b)], the low-energy response is strongly enhanced. The presence of the zero-frequency magnetic response in the vicinity of the incommensurate wave vector $Q \approx 0.14$ r.l.u. results in a nonzero NMR relaxation rate. We illustrate sensitivity of the spin pseudogap Δ_s to the magnetic criticality parameter λ by plotting in Fig. 3 the spectral function for two values of λ: $\lambda = 1$ (black) and $\lambda = 1.1$ (red). These values correspond to red and black squares on the phase diagram Fig. 1(b). Both in the SC and the N states the upper part of HG is not sensitive to the small variation of λ. Conversely, the lower part in the SC state $\omega < \Delta$ is very sensitive. Naturally, the spin pseudogap Δ_s is smaller at $\lambda = 1.1$ compared to that at $\lambda = 1$ since the former is closer to the phase boundary in Fig. 1(b).

Two-dimensional (q_x, q_y) color maps of the calculated structure factor corresponding to the "red" spectra in Fig. 3(a) are presented in Fig. 5. The maps are close to data for $La_{1.84}Sr_{0.16}CuO_4$ (Fig. 1 in Ref. [31]). Detail comparison shows that $La_{1.84}Sr_{0.16}CuO_4$ is slightly more critical. Increasing $\lambda = 1.1$ to $\lambda \approx 1.15$–1.2 we can even better reproduce data of Ref. [31] However, we do not perform the fit due to the reason explained in Sec. VIII.

IV. MAGNETIC CRITICALITY MECHANISM OF THE HOUR-GLASS DISPERSION

The results presented in the previous section indicate that the HG is driven by the SL Lifshitz magnetic criticality, SC plays a secondary role and leads to the spectral line narrowing in the lower part of HG. In order to elucidate this point, we plot in Fig. 6 denominators of the Green's function (3) versus q_x for $x = 0.16$. At $\omega = 0$ the denominator is real and Fig. 6(a) displays the $\omega = 0$ denominator in the SC state for three different values of λ. For $\lambda = 1.1$ and 1.25, the denominator is negative indicating stability of the SL phase. However, at $\lambda = 1.36$ the denominator vanishes, $D^{-1} = 0$, at $q_x \approx 0.135$ r.l.u. indicating condensation of the spin spiral with this wave vector [see the phase diagram Fig. 1(b)]. In Fig. 6(b) we plot the denominator in the SC state for $\omega = 0.15J$ and $\lambda = 1.1$, and in Fig. 6(c) we plot the same denominator but in the N state. In the SC state, the Green's function denominator is close to zero at $q_x \approx 0.12$ r.l.u. and this results in a narrow peak in the $\omega = 0.15J$ red curve in Fig. 3(a). In the N state the real part of the denominator is also small, but the imaginary part is large, thus the magnetic critical enhancement just results in a very broad structure in the $\omega = 0.15J$ red curve in Fig. 3(b).

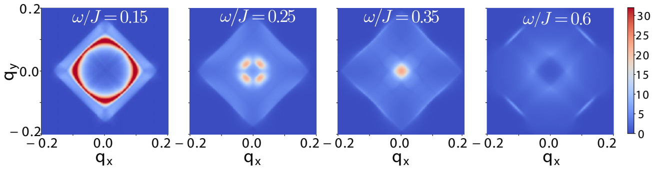

FIG. 5. Color maps of fixed energy (q_x, q_y) scans of magnetic spectral function $S(\omega, q)$ for $x = 0.16$ in SC phase. The magnetic criticality parameter $\lambda = 1.1$, the SL gap is $\Delta = 0.35J$, the SC gap is $\Delta_{SC} = 0.2J$.

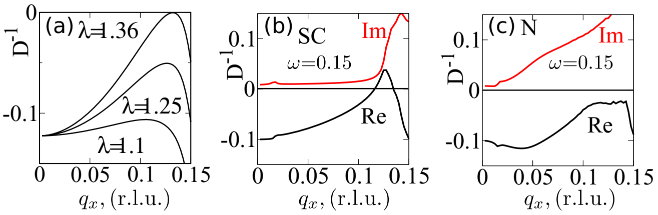

FIG. 6. Denominators of the Green's function (3) versus q_x for $x = 0.16$, $\Delta = 0.35J$, $\Delta_{SC} = 0.2J$. (a) SC state, $\omega = 0$, three different values of λ. (b) SC state, $\omega = 0.15J$, $\lambda = 1.1$, real (black) and imaginary (red) parts. (c) N state, $\omega = 0.15J$, $\lambda = 1.1$, real (black) and imaginary (red) parts.

Thus, the HG is a collective excitation driven by the Lifshitz magnetic criticality. The role of SC is just to suppress the decay rate of the collective excitation.

V. IS THERE A HOLLOW NECK IN THE HOUR GLASS?

Sometimes experimental HG dispersion is plotted with a hollow "neck" as it is shown in Fig. 4(b). We think that the hollow neck does not exist, but we understand how it can mistakenly arise in the analysis of experimental data. Figure 3(a) demonstrates pairs of narrow peaks for scans above and below the HG neck and a broad peak at the neck $\omega = \Delta = 0.35J$. An assumption that the broad peak consists of two narrow peaks leads to the hollow neck. However, we believe this is wrong, the neck of the HG is intrinsically broad. We believe that there is no hollow neck in HG.

VI. CALCULATED *q* SCANS OF THE SPECTRAL FUNCTION IN THE UNDERDOPED CASE: EMERGENT INCOMMENSURATE MAGNETIC ORDER

Next, we look at the lower doping $x = 0.1$. The SL gap according to Fig. 2(b) is $\Delta = 0.3J$. We keep the value of the magnetic criticality parameter unchanged, $\lambda = 1.1$, but the value of the SC gap is reduced, $\Delta_{SC} = 0.1J \approx 13$ meV (see Appendix C). Figure 7 presents calculated q_x scans of the spectral function for six values of ω. The red circle on the

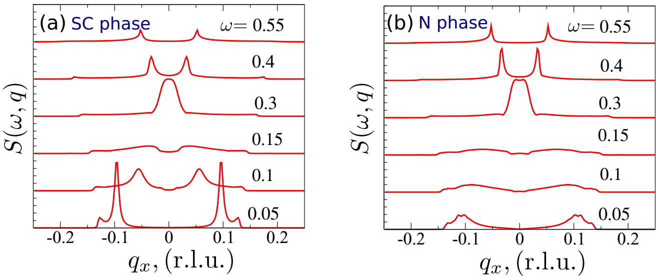

FIG. 7. Calculated momentum scans of the spectral function for $x = 0.1$, $\Delta = 0.3J$, $\Delta_{\mathrm{SC}} = 0.1J$, $\lambda = 1.1$, and six different energies. Energies in units of J are shown near the respective lines. (a) Corresponds to the SC state and (b) to the N state.

phase diagram Fig. 1(b) corresponding to these parameters is located close to the critical line. Therefore, the low-frequency response in Fig. 7 is strongly enhanced compared to that in Fig. 3. In this case, the spin pseudogap is practically zero, $\Delta_s \approx 0$. Moreover, the lower part of HG becomes evident even in the N state in agreement with the observation (O3). Further decreasing of doping would result in an emergent static incommensurate magnetic order in agreement with the observation (O5).

The HG dispersion deduced from Figs. 3(a) and 7(a) are plotted in Fig. 1(a) by the blue and red lines, respectively.

VII. WINE-GLASS DISPERSION

It is clear from the above discussion that decreasing of the magnetic criticality parameter λ reduces the intensity of the lower part of the HG. In Fig. 8 we present momentum scans for $\lambda = 0.9$. All other parameters are the same as that in Fig. 7, $x = 0.1$, $\Delta = 0.3J$, $\Delta_{\mathrm{SC}} = 0.1J$. The blue star on the phase diagram Fig. 1(b) corresponds to this set of parameters. In Fig. 8 the intensity in the lower part of the spectrum is dramatically reduced compared to that in Fig. 7. At the same time, the upper part of the spectrum is practically the same. Thus, reducing λ one drives the HG dispersion to the "wine-glass" regime reported in Refs. [11,15].

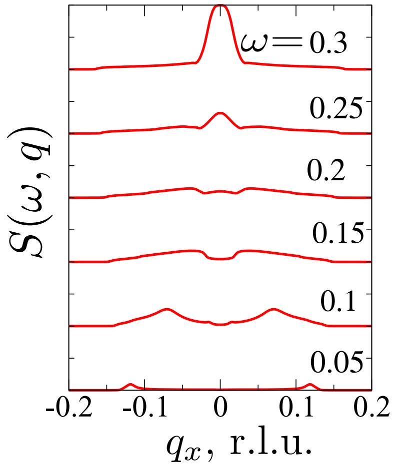

FIG. 8. Calculated momentum scans of the spectral function in the SC state for $x = 0.1$, $\Delta = 0.3J$, $\lambda = 0.9$, and six different energies. Energies in units of J are shown near the respective lines.

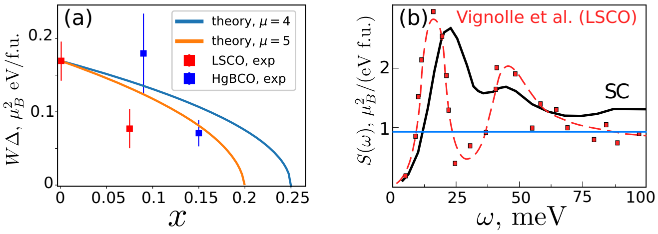

FIG. 9. (a) The SL sum rule $W\Delta = 0.5A\sqrt{1 - \mu x}$ [Eq. (5)] versus doping. Two theoretical curves indicate uncertainty of μ. The red points are extracted from $\mathrm{La}_{2-x}\mathrm{Sr}_x\mathrm{CuO}_4$ data [32] and the blue points from $\mathrm{HgBa}_2\mathrm{CuO}_{4+\delta}$ data [11,15]. (b) Black line represents theoretical q-integrated spectral function $S(\omega)$ for $x = 0.16$, $\Delta = 0.35J$, $\Delta_{\mathrm{SC}} = 0.2J$, $\lambda = 1.1$. The red line is experimental $S(\omega)$ for $\mathrm{La}_{1.84}\mathrm{Sr}_{0.16}\mathrm{CuO}_4$ [31]. The blue horizontal line shows $S(\omega)$ in $\mathrm{La}_2\mathrm{CuO}_4$.

VIII. LIFSHITZ SPIN-LIQUID FINGERPRINT RELATION

In the previous sections we have explained all the major HG observations (O1)–(O6) listed in the Introduction. Is there a further experimental confirmation of the developed theory? The answer is yes. The central point of the theory is that the Lifshitz SL is very similar to the parent antiferromagnet. Most explicitly, this point is reflected in Eqs. (4) and (5). The spectral weight W in the SL phase [Eq. (5)] is expressed via the coefficient A known from the parent antiferromagnet [Eq. (4)]. For this reason, we call Eq. (5) the Lifshitz SL "fingerprint" relation. Let us compare this relation with experimental data.

Using Eq. (4) and fitting the 5-K data in Fig. 4(a) of Ref. [32] for undoped $\mathrm{La}_2\mathrm{CuO}_4$ we find $A \approx 0.35\mu_B^2$ eV/f.u. Hence, using Eq. (5) we plot in Fig. 9(a) theoretical curves for the product $W \times \Delta$ versus doping. We know the value of the coefficient μ in (5) only approximately, therefore, we present curves for $\mu = 4, 5$ to indicate theoretical uncertainty. At the same, in Fig. 9(a) we present experimental points extracted from data for $\mathrm{La}_{2-x}\mathrm{Sr}_x\mathrm{CuO}_4$ (red) [32] and $\mathrm{HgBa}_2\mathrm{CuO}_{4+\delta}$ (blue) [11,15]. The red point at $x = 0$ gives the normalization of the theoretical curve. The agreement is quite good, the data are consistent with the SL "fingerprint" relation.

It would be very interesting to perform a similar analysis for $\mathrm{YBa}_2\mathrm{Cu}_3\mathrm{O}_{6.5}$ (YBCO). The compound has theoretical complications related to the double-layer structure and to the oxygen chains, but these issues are probably resolvable. The major problem is that there is not enough data with absolute normalization of intensity.

The next point we address is the q-integrated spectral function $S(\omega) = \int S(\omega, \boldsymbol{q}) \frac{d^2q}{(2\pi)^2}$. To be specific, we take the same set of parameters as that in Fig. 3, $x = 0.16$, $\Delta = 0.35J$, $\lambda = 1.1$, $\Delta_{\mathrm{SC}} = 0.2J$. The calculated spectral function in the SC state is shown in Fig. 9(b) by the black line. For normalization we use the value of A extracted from undoped $\mathrm{La}_2\mathrm{CuO}_4$ as described in the second paragraph of this section. In the same Fig. 9(b) we plot the experimental curve (red) for $\mathrm{La}_{1.84}\mathrm{Sr}_{0.16}\mathrm{CuO}_4$ [31]. The agreement between the theory and the experiment both in shape and in the absolute normalization is good. The characteristic double-hump structure has been also observed in $YBa_2Cu_3O_{6.5}$ [10]. As we pointed out above, a slight increase of criticality parameter $\lambda = 1.1 \to \lambda \approx 1.15$–$1.2$ would shift the low peak down close to the experimental position. In principle, one can try to fit the data by changing λ. However, there are recent evidences [33,34] indicating a phonon with energy $\omega \approx 18$–20 meV. The phonon adds some intensity to the lower peak in Fig. 9(b). Of course, the phonon is not described by our theory. This is why we do not fit data of Ref. [31] presented in Fig. 9(b).

According to Eq. (4), the q-integrated spectral function in the parent antiferromagnet is $S(\omega) = \frac{A}{8\pi J^2} \approx 0.95\mu_B^2/(\mathrm{eV\ \ f.u.})$. This value is shown in Fig. 9(b) by the blue horizontal line. In the energy interval above the neck of HG, $\omega = 50$–80 meV, this value coincides with $S(\omega)$ for $La_{1.84}Sr_{0.16}CuO_4$ presented in the same figure. This proves the point (F4) listed in the Introduction. The same point is true for YBCO. Relevant data are presented in Fig. 2(a) of Ref. [10]. Solid lines in this figure represent $S(\omega)$ in $YBa_2Cu_3O_{6.5}$ for three different temperatures and the horizontal dashed line shows $S(\omega)$ in the parent antiferromagnet [35]. From these data we conclude that in the interval $\omega = 50$–80 meV the structure factor $S(\omega)$ in $YBa_2Cu_3O_{6.5}$ and in the parent antiferromagnet has the same value.

IX. CONCLUSIONS

We show that the hour-glass magnetic dispersion in underdoped cuprates is driven by properties of the Lifshitz magnetic critical spin liquid. Superconductivity plays a secondary role and only responsible for the narrowing of the spectral lines. We list the six major observations related to the hour-glass dispersion and explain all of them. We propose a spin-liquid "fingerprint relation" and demonstrate that neutron scattering data support the relation.

ACKNOWLEDGMENTS

We thank G. Khaliullin for stimulating discussions. We also thank P. Bourges, M. Fujita, M. Greven, S. M. Hayden, B. Keimer, J. M. Tranquada, and C. Ulrich for discussions and important communications. The work has been supported by Australian Research Council Grant No. DP160103630.

APPENDIX A: EFFECTIVE ACTION

1. Extended *t-J* model

The Hamiltonian of the extended t-J model reads as [36–38]

$$H = -t\sum_{\langle ij\rangle} c^\dagger_{i,\sigma}c_{j,\sigma} - t'\sum_{\langle\langle ij\rangle\rangle} c^\dagger_{i,\sigma}c_{j,\sigma} - t''\sum_{\langle\langle\langle ij\rangle\rangle\rangle} c^\dagger_{i,\sigma}c_{j,\sigma} + J\sum_{\langle i,j\rangle}\left[\boldsymbol{S}_i\cdot\boldsymbol{S}_j - \frac{1}{4}N_iN_j\right], \tag{A1}$$

where $c^\dagger_{i\sigma}$ $(c_{i\sigma})$ is the creation (annihilation) operator for an electron with spin $\sigma = \uparrow,\downarrow$ at Cu site i; the operator of electron spin reads as $\boldsymbol{S}_i = \frac{1}{2}c^\dagger_{i\alpha}\boldsymbol{\sigma}_{\alpha\beta}c_{i\beta}$. The electron number density operator is $N_i = \sum_\sigma c^\dagger_{i\sigma}c_{i\sigma}$, where x is the hole doping, so that the sum rule $\langle N_i\rangle = 1 - x$ is obeyed. In addition to Hamiltonian (A1) there is the no-double-occupancy constraint, which accounts for a strong electron-electron onsite repulsion. The value of superexchange is approximately the same for all cuprates, $J \approx 125$ meV. The superexchange has been directly measured and shown to be independent of doping [25]. While in Eq. (A1) we present only three hopping matrix elements, the nearest-site hopping t, the next-nearest-site hopping t', and the next-next-nearest-site hopping t'', we know from LDA calculations [28] that more distant hoppings, $t^{(3)}$, $t^{(4)}$, and even $t^{(5)}$, are also significant. Unfortunately, values of the hopping matrix elements cannot be directly measured. It is widely believed that the value $t \approx 400$ meV $\approx 3J$ is reliable and common for all cuprates, we use this value in this work. However, values of the distant hopping matrix elements are rather uncertain and can vary from one family to another.

The Fermi surface of a lightly doped extended t-J model consists of Fermi pockets shown in Fig. 2(a) and centered at the nodal points $\mathbf{k}_0 = (\pm\pi/2, \pm\pi/2)$, and $\mathbf{k}_0 = (\pm\pi/2, \mp\pi/2)$. The single-hole dispersion can be parametrized as [39]

$$\begin{aligned}\epsilon_{\boldsymbol{k}} &= \beta_1(\gamma_{\boldsymbol{k}}^+)^2 + \beta_2(\gamma_{\boldsymbol{k}}^-)^2, \quad \gamma_{\boldsymbol{k}}^{\pm} = \frac{1}{2}(\cos k_x \pm \cos k_y),\\ \epsilon_{\boldsymbol{k}} &\approx \beta_1\frac{p_1^2}{2} + \beta_2\frac{p_2^2}{2}.\end{aligned} \tag{A2}$$

Here, $\mathbf{p} = \mathbf{k} - \mathbf{k}_0$ [see Fig. 2(a)]. We set the lattice spacing equal to unity $a = 3.81$ Å $\to 1$. The second line in Eq. (A2) corresponds to the quadratic expansion of the fermion dispersion in the vicinity of the centers of Fermi pockets. The ellipticity of the holon pocket is $\sqrt{\beta_1/\beta_2}$. The Fermi energy is related to doping as

$$\begin{aligned}\epsilon_F &\approx \pi\beta x,\\ \beta &= \sqrt{\beta_1\beta_2} = \frac{1}{m^*}.\end{aligned} \tag{A3}$$

Values of the inverse effective masses β_1, β_2 follow from Hamiltonian (A1). They have been calculated using self-consistent Born approximation (SCBA) (see Refs. [39,40]). The values strongly depend on distant hopping parameters which are essentially unknown, even $t^{(3)}$-$t^{(5)}$ significantly influence SCBA results. For illustration we present here values of β_1, β_2 obtained for several sets of the distant hopping parameters. We consider only the sets that result in positive β_1 and β_2. For the "pure" t-J model, $t' = t'' = t^{(3)} = t^{(4)} = t^{(5)} = 0$, the values are $\beta_1 = 1.96J$, $\beta_2 = 0.30J$. For the set $t' \approx 0.23J$, $t'' = 0$, $t^{(3)} = t^{(4)} = t^{(5)} = 0$ one gets the Van Hove singularity $\beta_2 = 0$. On the other hand, in the limit $t'' \gg t', J$ the inverse masses are very large $\beta_1 \approx \beta_2 \approx 8t'' \gg J$. For the middle of the LDA range [28], $t' = -0.5J$, $t'' = 0.5J$, $t^{(3)} = t^{(4)} = t^{(5)} = 0$ the inverse masses are $\beta_1 \approx 2.76J$, $\beta_2 \approx 2.62J$. While we can claim that $\beta = \sqrt{\beta_1\beta_2} \sim 2$, the so strong dependence on unknown parameters indicates that in the end the effective masses and especially the ellipticity of the Fermi pocket have to be taken from experiment.

Even more important than the effective masses is the dimensionless magnetic criticality parameter [22,40]

$$\lambda = \frac{8g^2}{\pi\sqrt{\beta_1\beta_2}}. \tag{A4}$$

Here, $g = Zt$ is the magnon-holon coupling constant, Z is the holon quasiparticle residue. In theory by varying t' and t'' one can vary λ from zero to infinity. In the large-t'' limit, $t'' \gg t', J$, the parameter is very small, $\lambda \to 0$. On the other hand, near the Van Hove singularity $\beta_2 \to 0$, the parameter is very large $\lambda \to \infty$. For the "pure" t-J model, $t' = t'' = t^{(3)} = t^{(4)} = t^{(5)} = 0$ the criticality parameter value is $\lambda = 2.51$. For the middle of the LDA range [28], $t' = -0.5J$, $t'' = 0.5J$, $t^{(3)} = t^{(4)} = t^{(5)} = 0$, the criticality parameter value is $\lambda = 1.1$. Within the overall LDA range of the hopping parameters [28], λ varies from 1 to 2. Numerically, the difference between $\lambda = 2$ and 1 is not that large, but physically the difference is enormous. The value $\lambda \geqslant 2$ implies that the system is unstable with respect to the phase separation (see Refs. [40,41]). So, the "pure" t-J model with $\lambda \approx 2.5$ is unstable and hence inconsistent with experiment. On the other hand, the value $\lambda = 1$ corresponds to the stable spin-liquid phase which is perfectly consistent with experiment [see Fig. 1(b) and Ref. [16]]. While from LDA+SCBA we can claim that $\lambda \sim 1$, the strong dependence on unknown parameters indicates that in the end the value of λ must be taken from experiment. Based on the phase diagram Fig. 1(b), we see that values $0.8 < \lambda < 1.3$ are generally consistent with data.

To summarize this section: We base our analysis on the extended t-J model and use the value $J \approx 125$ meV known from experiment. In the calculation we use the value $t = 3J$, we have checked that a variation of t within $2.5J < t < 3.5J$ influences our results very weakly. However, a variation of distant hopping matrix elements t', t'', $t^{(3)}, \ldots$ have an enormous effect on physics. Variation of these matrix elements within the window given by LDA calculations [28] can drive the system from the Néel state through the spin-liquid state to the spin spiral state and even to the phase separation. Based on the spin-liquid theory, we conclude that the range $0.8 < \lambda < 1.3$ is consistent with experimental observations, so in our calculations we use this range. Specifically in the paper we present results for $\lambda = 1.1$, 1, and 0.9 to demonstrate sensitivity to the criticality parameter. The value of the effective mass is less important, in the paper we present results for $\beta = \sqrt{\beta_1\beta_2} = 2J$ ($m^* = 2.1m_e$) and $\beta_1/\beta_2 = 6$. We have checked that the set $\beta = \sqrt{\beta_1\beta_2} = 3J$ and $\beta_1/\beta_2 = 4$ results in practically the same answers.

2. Quantum field theory: The low-energy limit of the extended *t*-*J* model

While the t-J model is the low-energy reduction of the three-band Hubbard model, the total energy range in the t-J model $\Delta\epsilon \sim 8t \sim 24J \approx 3$ eV is still very large. Account for quantum fluctuations at lower energy scales practically unavoidably requires a quantum field theory approach. Theoretical arguments explaining this point have been discussed in several theoretical papers including our recent work [16].

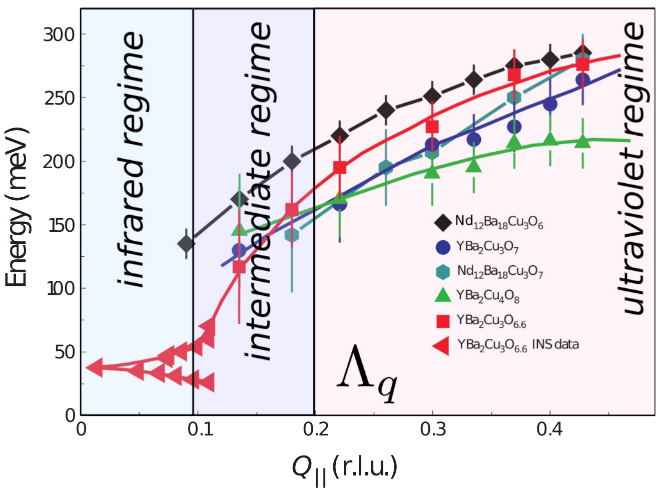

FIG. 10. Magnetic dispersion along the (1,0) direction. Points show combined data on resonant inelastic x-ray scattering and inelastic neutron scattering in NdBCO and YBCO at $T = 15$ K [26]. Vertical lines separate three different regimes that we call "infrared regime," "intermediate regime," and "ultraviolet regime."

Here, we repeat only experimental arguments supporting this statement. In Fig. 10 we present magnetic dispersion along the (1,0) direction taken from Ref. [26]. The dispersion is based on combined data on resonant inelastic x-ray scattering and inelastic neutron scattering. The data indicate three distinct regimes separated in Fig. 10 by vertical lines. In the "ultraviolet regime" the dispersion only very weakly depends on doping, practically independent. This is where our "fact" (F2) in the Introduction comes from. In the "intermediate regime" there is a significant softening with doping and the most dramatic doping dependence takes place in the "infrared regime." The low-energy effective field theory is relevant to the "infrared" and the "intermediate" regimes. In these regimes, energies of magnetic excitations and energies of holons are small, $\omega, \epsilon < 2J$. On the other hand, in the "ultraviolet regime" the energies are large, $\omega \sim 2J$ and $8t > \epsilon \gtrsim 2J$. The field theory has the ultraviolet cutoff Λ_q which is the upper edge of the "intermediate regime" as it is indicated in Fig. 10. The value of the cutoff that follows from the data is $\Lambda_q \sim 0.2$ r.l.u. The same value follows from the theory (see Ref. [16]).

The low-energy Lagrangian of the t-J model was first derived in Ref. [24] with some important terms missing. The full effective Lagrangian was derived in Ref. [22]. This approach necessarily requires an introduction of two checkerboard sublattices, independent of whether there is a long-range antiferromagnetic (AFM) order or the order does not exist. The two checkerboard sublattices allow us to avoid a double counting of quantum states in the case when spin and charge are separated. A holon carries charge and does not carry spin, but it can be located at one of the sublattices and this is described by the pseudospin $\frac{1}{2}$. Due to the checkerboard sublattices, the Brillouin zone coincides with magnetic Brillouin zone (MBZ) even in the absence of a long-range AFM order. Therefore, there are four half-pockets in Fig. 2(a) or two full pockets within MBZ. Finally, the Lagrangian reads as [22]

$$\mathcal{L} = \frac{\chi_\perp}{2}\dot{\vec{n}}^2 - \frac{\rho_s}{2}(\nabla\vec{n})^2 + \sum_\alpha \left\{ \frac{i}{2}[\psi_\alpha^\dagger \mathcal{D}_t \psi_\alpha - (\mathcal{D}_t\psi_\alpha)^\dagger \psi_\alpha] \right.$$
$$\left. - \psi_\alpha^\dagger \epsilon_\alpha(\mathcal{P})\psi_\alpha + \sqrt{2}g(\psi_\alpha^\dagger \vec{\sigma}\psi_\alpha)\cdot[\vec{n}\times(\boldsymbol{e}_\alpha\cdot\nabla)\vec{n}] \right\}. \tag{A5}$$

Fermions (holons) are described by a spinor ψ_α with the pseudospin $\frac{1}{2}$, and the vector of staggered magnetization $\boldsymbol{n}$ normalized as $\boldsymbol{n}^2 = 1$ corresponds to localized spins at Cu sites. The first line in (A5) is $O(3)$ nonlinear sigma model that describes spin dynamics, the second line is the Lagrangian for noninteracting holons. The long covariant derivatives in Eq. (A5) are defined as

$$\boldsymbol{P} = -i\nabla + \tfrac{1}{2}\vec{\sigma}\cdot[\vec{n}\times\nabla\vec{n}], \quad \mathcal{D}_t = \partial_t + \tfrac{1}{2}\vec{\sigma}\cdot[\vec{n}\times\partial_t\vec{n}].$$

The index $\alpha = 1, 2$ enumerates two full holon pockets in Fig. 2(a). The term in the bottom line in Eq. (A5) describes the coupling between holons and the staggered magnetization. Pauli matrices $\boldsymbol{\sigma}$ in Eq. (A5) act on the holon's pseudospin and $\boldsymbol{e}_\alpha = 1/\sqrt{2}(1, \pm 1)$ denotes a unit vector orthogonal to the face of the MBZ where the holon is located. The coupling constant g enters Eq. (A4).

The Lagrangian (A5) is fully equivalent to the t-J model Hamiltonian (A1). In essence, Eq. (A5) originates from the Hamiltonian (A1) rewritten in notations convenient for analysis of the low-energy physics. The relation between (A5) and (A1) is the same as that between the nonlinear σ model and the Heisenberg antiferromagnetic model on square lattice. The Lagrangian (A5) contains five parameters, $\chi_\perp$, ρ_s, β_1, β_2, and g. Of course they can be expressed in terms of parameters of the "parent" t-J model. We have already discussed β_1 and β_2. The coupling $g = Zt$ is related to λ [see Eq. (A4)], so it is also already discussed. In the limit $x \to 0$ the σ-model parameters $\chi_\perp$ and ρ_s coincide with that of the 2D Heisenberg model on the square lattice, $\chi_\perp = 1/8J$, $\rho_s = J/4$, up to an overall scalar prefactor in Lagranian (A5) due to the renormalization of the spin magnitude by quantum fluctuations. The magnon speed is

$$c_0 = \sqrt{\rho_s/\chi_\perp} = \sqrt{2}J. \tag{A6}$$

3. Dependence of the Lagrangian parameters on doping

The small parameter of our theory is doping $x \ll 1$. The Lagrangian parameters in Appendix A 2 are written in the limit $x \to 0$. Here, we discuss the x dependence of the parameters up to the linear in x approximation. The first effect is renormalization of the σ-model parameters due to fermionic fluctuations at the high-energy scale $E \sim 8t \sim 24J$ (see Ref. [16]):

$$\begin{aligned} \chi_\perp &= \frac{1}{8J} \to \frac{1}{8J}, \\ \rho_s &= \frac{J}{4} \to \frac{J}{4}(1-\mu x), \\ c &= \sqrt{\frac{\rho_s}{\chi_\perp}} \to c_0\sqrt{1-\mu x}. \end{aligned} \tag{A7}$$

Note that the numerical coefficient $\mu \approx 4$ in the doping-dependent prefactor is known only approximately (see Ref. [16]).

The magnon Green's function generated by (A5) above the spin-liquid energy scale Δ, $\Delta < \omega \lesssim J$ after taking into account Eqs. (A7) reads as

$$D(\omega, \boldsymbol{q}) \propto \frac{\chi_\perp^{-1}}{\omega^2 - c_0^2(1-\mu x)\boldsymbol{q}^2 + i0}. \tag{A8}$$

Hence, the sum rule for the spin structure factor is

$$\int S(\omega, \boldsymbol{q}) d\omega\, d^2q \propto \int \mathrm{Im} D(\omega, \boldsymbol{q}) d\omega\, d^2q \propto \frac{\Lambda_q}{\sqrt{1-\mu x}}. \tag{A9}$$

The integration is performed in limits $0 < \omega < \infty$, $0 < q < \Lambda_q$, where $\Lambda_q \approx 1.2 \approx 2\pi * 0.2$ (r.l.u.) (we remind that we set the lattice spacing equal to unity) is the ultraviolet cutoff of the theory. Equation (A9) implies that the spin sum rule is increasing with doping. Obviously, the sum rule should be a doping-independent constant. This implies that magnetic fluctuations at the scale $\omega \sim J \gg \Delta$ must generate the magnon quasiparticle residue

$$Z_x = \sqrt{1-\mu x}. \tag{A10}$$

Equations (A8) and (A9) must be multiplied by the residue and this makes the sum rule doping independent.

APPENDIX B: THE FRUSTRATION MECHANISM BEHIND THE LIFSHITZ SPIN LIQUID

Here, we explain the mechanism of the Lifshitz SL without going to technical details. The details are presented in Ref. [16]. The easiest way to understand how the Lifshitz SL arises due to frustration of spins by mobile holons is to stay in the Néel phase, $\lambda < 1$, and to increase λ [see the phase diagram Fig. 1(b)]. In the Néel phase there is a collinear long-range order $\langle n_z \rangle \neq 0$, and there is a quantum fluctuation $\langle n_\perp^2 \rangle = \langle n_x^2 \rangle + \langle n_y^2 \rangle$. A calculation at small doping x gives the following answer for the fluctuation:

$$\langle \vec{n}_\perp^2 \rangle = \frac{x\beta}{2\rho_s} \ln\left(\frac{1}{1-\lambda}\right) + \text{const.} \tag{B1}$$

When λ is sufficiently close to unity, the fluctuation is very large and this results in the quantum melting of the long-range Néel order. This explains the Néel-Lifshitz SL transition line in Fig. 1(b). Similar arguments lead the Lifshitz SL–spin spiral transition line on the phase diagram (see Ref. [16]).

APPENDIX C: EFFECT OF SUPERCONDUCTIVITY

With account of Z_x, the magnetic Green's function in the SL phase reads as [16]

$$\begin{aligned} D(\omega, \boldsymbol{q}) &= -i \int d^2r\, dt\, e^{i\omega t + iqr} \langle T\{\boldsymbol{n}_i(\boldsymbol{r}, t)\cdot \boldsymbol{n}_i(0,0)\}\rangle \\ &= \frac{2}{\chi_\perp}\frac{Z_x}{\omega^2 - c^2q^2 - \Delta^2 - \Pi(\omega, \boldsymbol{q}) + i0}. \end{aligned} \tag{C1}$$

Here, Δ is the SL gap and $\Pi(\omega, q)$ is the magnon polarization operator (fermionic loop). The magnon-holon interaction is given by the Lagrangian (A5). Hence, a calculation of the magnon polarization operator is relatively straightforward. In the calculation, one can disregard superconducting pairing of holons or alternatively take the pairing into account. Results without the pairing we call the "normal-state results."

In this work we introduce superconductivity in the theory *ad hoc* via the phenomenological d-wave SC gap. We use the simplest parametrization for the gap

$$\Delta_{\boldsymbol{k}} = \Delta_{\mathrm{SC}}\gamma_{\boldsymbol{k}}^{-}. \tag{C2}$$

In our numerical calculations we used the following values of the SC gap:

$$\begin{aligned} x = 0.16: &\quad \Delta_{\mathrm{SC}} = 0.2J,\\ x = 0.10: &\quad \Delta_{\mathrm{SC}} = 0.1J. \end{aligned} \tag{C3}$$

Expressed in terms of parameters of the Lagrangian (A5), the zero-temperature polarization operator in the SC phase reads as [42]

$$\begin{aligned} \Pi(\omega, q) = {}& \frac{2\pi\lambda c^2}{m^*}\sum_{\alpha=1,2} q_\alpha^2 \int \frac{d^2k}{(2\pi)^2}\{v_{\boldsymbol{k}}^2 u_{\boldsymbol{k+q}}^2 + u_{\boldsymbol{k}} v_{\boldsymbol{k}} u_{\boldsymbol{k+q}} v_{\boldsymbol{k+q}}\}\\ &\times\left[\frac{1}{\omega - E_{\boldsymbol{k}} - E_{\boldsymbol{k+q}} + i0} + (\omega \to -\omega)\right], \end{aligned} \tag{C4}$$

where $q_\alpha = \boldsymbol{q}\cdot\boldsymbol{e}_\alpha$ and $u_{\boldsymbol{k}}$ and $v_{\boldsymbol{k}}$ are Bogoliubov parameters:

$$\begin{aligned} u_{\boldsymbol{k}} &= \sqrt{\frac{1}{2}\left(1 + \frac{\xi_{\boldsymbol{k}}}{E_{\boldsymbol{k}}}\right)},\\ v_{\boldsymbol{k}} &= \mathrm{sign}(\gamma_{\boldsymbol{k}}^{-})\sqrt{\frac{1}{2}\left(1 - \frac{\xi_{\boldsymbol{k}}}{E_{\boldsymbol{k}}}\right)}. \end{aligned} \tag{C5}$$

The quasiparticle dispersion reads as

$$E_{\boldsymbol{k}} = \sqrt{\Delta_{\boldsymbol{k}}^2 + \xi_{\boldsymbol{k}}^2}, \quad \xi_{\boldsymbol{k}} = \epsilon_{\boldsymbol{k}} - \mu, \tag{C6}$$

where the chemical potential μ is defined by the condition

$$x = 2\sum_{\alpha=1,2}\int \frac{d^2k}{(2\pi)^2} v_{\boldsymbol{k}}^2. \tag{C7}$$

Numerical evaluation of the polarization operator (C4) is straightforward and we use it in this work.

[1] M. Arai, T. Nishijima, Y. Endoh, T. Egami, S. Tajima, K. Tomimoto, Y. Shiohara, M. Takahashi, A. Garrett, and S. M. Bennington, Phys. Rev. Lett. **83**, 608 (1999).

[2] P. Bourges, Y. Sidis, H. F. Fong, L. P. Regnault, J. Bossy, A. Ivanov, and B. Keimer, Science **288**, 1234 (2000).

[3] S. M. Hayden, H. A. Mook, P. Dai, T. G. Perring, and F. Dogan, Nature (London) **429**, 531 (2004).

[4] J. M. Tranquada, H. Woo, T. G. Perring, H. Goka, G. D. Gu, G. Xu, M. Fujita, and K. Yamada, Nature (London) **429**, 534 (2004).

[5] V. Hinkov, P. Bourges, S. Pailhes, Y. Sidis, A. Ivanov, C. D. Frost, T. G. Perring, C. T. Lin, D. P. Chen, and B. Keimer, Nat. Phys. **3**, 780 (2007).

[6] M. Fujita, H. Hiraka, M. Matsuda, M. Matsuura, J. M. Tranquada, S. Wakimoto, G. Xu, and K. Yamada, J. Phys. Soc. Jpn. **81**, 011007 (2012).

[7] M. Vojta, T. Vojta, and R. K. Kaul, Phys. Rev. Lett. **97**, 097001 (2006).

[8] Hung Fai Fong, B. Keimer, P. W. Anderson, D. Reznik, F. Dogan, and I. A. Aksay, Phys. Rev. Lett. **75**, 316 (1995).

[9] H. F. Fong and B. Keimer, D. L. Milius, and I. A. Aksay, Phys. Rev. Lett. **78**, 713 (1997).

[10] P. Bourges, H. F. Fong, L. P. Regnault, J. Bossy, C. Vettier, D. L. Milius, and I. A. Aksay, and B. Keimer, Phys. Rev. B **56**, R11439 (1997).

[11] M. K. Chan, C. J. Dorow, L. Mangin-Thro, Y. Tang, Y. Ge, M. J. Veit, G. Yu, X. Zhao, A. D. Christianson, J. T. Park, Y. Sidis, P. Steffens, D. L. Abernathy, P. Bourges, and M. Greven, Nat. Commun. **7**, 10819 (2016).

[12] I. Kapon, D. S. Ellis, G. Drachuck, G. Bazalitski, E. Weschke, E. Schierle, J. Strempfer, C. Niedermayer, and A. Keren, Phys. Rev. B **95**, 104512 (2017).

[13] K. Yamada, C. H. Lee, K. Kurahashi, J. Wada, S. Wakimoto, S. Ueki, H. Kimura, Y. Endoh, S. Hosoya, G. Shirane, R. J. Birgeneau, M. Greven, M. A. Kastner, and Y. J. Kim, Phys. Rev. B **57**, 6165 (1998).

[14] D. Haug, V. Hinkov, Y. Sidis, P. Bourges, N. B. Christensen, A. Ivanov, T. Keller, C. T. Lin, and B. Keimer, New J. Phys. **12**, 105006 (2010).

[15] M. K. Chan, Y. Tang, C. J. Dorow, J. Jeong, L. Mangin-Thro, M. J. Veit, Y. Ge, D. L. Abernathy, Y. Sidis, P. Bourges, and M. Greven, Phys. Rev. Lett. **117**, 277002 (2016).

[16] Y. A. Kharkov and O. P. Sushkov, Phys. Rev. B **98**, 155118 (2018).

[17] Ar. Abanov, A. V. Chubukov, M. Eschrig, M. R. Norman, and J. Schmalian, Phys. Rev. Lett. **89**, 177002 (2002).

[18] F. Onufrieva and P. Pfeuty, Phys. Rev. B **65**, 054515 (2002).

[19] A. Sherman and M. Schreiber, Phys. Rev. B **68**, 094519 (2003).

[20] I. Eremin, D. K. Morr, A. V. Chubukov, K. H. Bennemann, and M. R. Norman, Phys. Rev. Lett. **94**, 147001 (2005).

[21] M. V. Eremin, I. M. Shigapov, and I. M. Eremin, Eur. Phys. J. B **85**, 131 (2012).

[22] A. I. Milstein and O. P. Sushkov, Phys. Rev. B **78**, 014501 (2008).

[23] A. J. A. James and R. M. Konik, and T. M. Rice, Phys. Rev. B **86**, 100508(R) (2012).

[24] B. I. Shraiman and E. D. Siggia, Phys. Rev. B **42**, 2485 (1990).

[25] T. Imai, C. P. Slichter, K. Yoshimura, and K. Kosuge, Phys. Rev. Lett. **70**, 1002 (1993).

[26] M. Le Tacon, G. Ghiringhelli, J. Chaloupka, M. Moretti Sala, V. Hinkov, M. W. Haverkort, M. Minola, M. Bakr, K. J. Zhou, S. Blanco-Canosa, C. Monney, Y. T. Song, G. L. Sun, C. T. Lin, G. M. De Luca, M. Salluzzo, G. Khaliullin, T. Schmitt, L. Braicovich, and B. Keimer, Nat. Phys. **7**, 725 (2011).

[27] P. W. Anderson, P. A. Lee, M. Randeria, T. M. Rice, N. Trivedi, and F. C. Zhang, J Phys.: Condens. Matter **16**, R755 (2004).

[28] O. K. Andersen, A. I. Liechtenstein, O. Jepsen, and F. Paulsen, J. Phys. Chem. Solids **56**, 1573 (1995); E. Pavarini, I. Dasgupta, T. Saha-Dasgupta, O. Jepsen, and O. K. Andersen, Phys. Rev. Lett. **87**, 047003 (2001).

[29] L. Taillefer, Annu. Rev. Condens. Matter Phys. **1**, 51 (2010).

[30] In the SC state we set temperature $T = 0$ and account for the SC gap. In the N state we set the SC gap equal to zero, but still have $T = 0$. This implies that our N state corresponds to the state with T just above T_c.

[31] B. Vignolle, S. M. Hayden, D. F. McMorrow, H. M. Rønnow, B. Lake, C. D. Frost, and T. G. Perring, Nat. Phys. **3**, 163 (2007).

[32] M. Matsuura, S. Kawamura, M. Fujita, R. Kajimoto, and K. Yamada, Phys. Rev. B **95**, 024504 (2017).

[33] J. J. Wagman, D. Parshall, M. B. Stone, A. T. Savici, Y. Zhao, H. A. Dabkowska, and B. D. Gaulin, Phys. Rev. B **91**, 224404 (2015).

[34] Zhijun Xu, C. Stock, Songxue Chi, A. I. Kolesnikov, Guangyong Xu, Genda Gu, and J. M. Tranquada, Phys. Rev. Lett. **113**, 177002 (2014).

[35] In Ref. [10] the value of $S(\omega)$ for the parent antiferromagnet is overestimated by 20%–30%. P. Bourges (private communication).

[36] P. W. Anderson, Science **235**, 1196 (1987).

[37] V. J. Emery, Phys. Rev. Lett. **58**, 2794 (1987).

[38] F. C. Zhang and T. M. Rice, Phys. Rev. B **37**, 3759 (1988).

[39] O. P. Sushkov, G. A. Sawatzky, R. Eder, and H. Eskes, Phys. Rev. B **56**, 11769 (1997).

[40] O. P. Sushkov and V. N. Kotov, Phys. Rev. B **70**, 024503 (2004).

[41] A. V. Chubukov and K. A. Musaelian, Phys. Rev. B **51**, 12605 (1995).

[42] O. P. Sushkov, Phys. Rev. B **54**, 9988 (1996).